Efficient Near-Infrared Harvesting in Perovskite-Organic Tandem Solar Cells

Zhenrong Jia[1,2,7], Xiao Guo[1,2,7], Xinxing Yin[3,7], Ming Sun[4], Jiawei Qiao[4], Xinyu Jiang[5], Xi Wang[1,2], Yuduan Wang[1,2], Zijing Dong[1,2], Zhuojie Shi[1,2], Chun-Hsiao Kuan[6], Jingcong Hu[1,2], Qilin Zhou[1,2], Xiangkun Jia[1,2], Jinxi Chen[1,2], Zhouyin Wei[2], Shunchang Liu[1,2], Haoming Liang[1,2], Nengxu Li[1,2], Ling Kai Lee[2], Renjun Guo[2], Stephan V. Roth[5], Peter Müller-Buschbaum[7], Xiaotao Hao[4], Xiaoyan Du[4], Yi Hou[1,2]*

[1]Department of Chemical and Biomolecular Engineering, National University of Singapore, Singapore, 117585, Singapore

[2]Solar Energy Research Institute of Singapore (SERIS), National University of Singapore, Singapore, 117574, Singapore

[3]China-Australia Institute for Advanced Materials and Manufacturing (IAMM), Jiaxing University, Jiaxing 314001, China

[4]School of Physics, State Key Laboratory of Crystal Materials, Shandong University, Jinan, 250100, P. R. China

[5]Deutsches Elektronen-Synchrotron (DESY), Notkestrasse 85, 22607 Hamburg, German

[6]Department of Applied Chemistry, and Institute of Molecular Science National Yang Ming Chiao Tung University 1001 Ta-Hseuh Rd., Hsinchu 300093, Taiwan

[7]Technical University of Munich, TUM School of Natural Sciences, Department of Physics, Chair for Functional Materials, James-Franck-Strasse 1, 85748 Garching, Germany

[7]These authors contributed equally.

*Correspondence to email: yi.hou@nus.edu.sg (Y.H.)

Abstract

The broad bandgap tunability of both perovskites and organic semiconductors enables the development of perovskite/organic tandem solar cells with promising theoretical efficiency. However, the certified efficiencies of reported perovskite-organic tandem solar cells remain lower than those of single-junction perovskite solar cells, primarily due to insufficient near-infrared photocurrent in narrow-bandgap organic sub-cell[1-3]. Here, we design and synthesize an asymmetric non-fullerene acceptor, P2EH-1V, featuring a unilateral conjugated π-bridge to reduce the optical bandgap to 1.27 eV while maintaining ideal exciton dissociation and nanomorphology. Transient absorption spectroscopy confirms efficient hole transfer from P2EH-1V to the donor PM6. Devices based on P2EH-1V exhibit reduced non-radiative voltage losses of 0.20 eV without compromising charge generation efficiency. We achieve a 17.9% efficiency for the organic bottom cell, with a high short-circuit current density (J_{sc}) of 28.60 mA cm^{-2}. Furthermore, we minimize interface recombination losses, enabling the perovskite top cell to achieve an impressive open-circuit voltage (V_{oc}) of 1.37 V and a fill factor (FF) of 85.5%. These advancements result in perovskite-organic tandem solar cells achieving a record efficiency of 26.7% (certified at 26.4%) over an aperture area greater than 1 cm^2.

Main

Non-fullerene acceptors (NFAs) used in organic photovoltaics (OPV) exhibit robust near-infrared absorption and significant bandgap tunability, making them ideal candidates for bottom cells in perovskite-organic tandem solar cells when paired with wide bandgap perovskite top cells[4-5]. This all-thin-film tandem configuration not only surpasses the Shockley-Queisser (S-Q) limit of both single-junction perovskite and organic photovoltaic cells but also offers enhanced operational stability due to the ultraviolet-filtering properties of the perovskite layer[6-9]. Compared to perovskite-silicon, perovskite-CIGS, and perovskite-perovskite tandems, the absorber layers of the two subcells in perovskite-organic tandems can be fully processed using high-throughput roll-to-roll techniques under consistent ambient conditions on flexible polymer substrates. Their lightweight and potentially flexible design make them particularly well-suited for applications such as building-integrated photovoltaics (BIPV), vehicle-integrated photovoltaics (VIPV), drones, and consumer electronics[10].

Despite these advances, the highest-performing perovskite-organic tandem solar cells to date still fall short of achieving higher certified power conversion efficiencies (PCEs) compared to published single-junction perovskite cells (24.7%) and other reported perovskite thin-film tandems, such as perovskite-perovskite (28.2%) and perovskite-CIGS tandems (24.2%), within the same active area (e.g., 1 cm^2)[11-14]. A significant challenge in advancing perovskite-organic tandems is the limited availability of efficient narrow-bandgap NFAs suitable for the organic bottom cell, which contributes to the relatively low photocurrent densities observed in these tandem devices[15-16]. For instance, the currently dominant acceptor, Y6 (BTP-4F), used in the bottom cell of perovskite-organic tandems, has an optical bandgap of approximately 1.33 eV. While

this bandgap is ideal for single-junction solar cells, it is suboptimal for tandem configurations, where the ideal bandgap for the bottom cell in dual-junction tandems is around 1.00 eV[18].

In previous studies, the bandgap of NFAs has been reduced by increasing the conjugation length or enhancing the intramolecular charge transfer effect[19-20]. However, constructing narrow-bandgap NFAs typically requires significantly extending the conjugated backbone, which sharply increases the highest occupied molecular orbital (HOMO) energy levels[21-22]. This approach leads to an energy level mismatch between the acceptors and polymer donors, negatively impacting exciton dissociation efficiency and overall external quantum efficiency (EQE) [23-24]. In this study, we design and synthesize a novel asymmetric NFA, P2EH-1V, by strategically inserting an ethylene double bond π-bridge between the central fused ring unit and the end groups of P2EH. This modification reduces the optical bandgap of the NFA to 1.27 eV while maintaining a sufficient energy level difference with the high-efficiency donor PM6, ensuring efficient exciton separation.

NFA design and photovoltaic performance

To realize an optimal NFA for the application in the perovskite-organic tandem solar cells, inserting the double bonds π-bridge into the NFAs is an effective strategy. Li et al. reported an ultra-narrow bandgap NFA with double bonds π-bridge, achieving a bandgap below 1.2 eV and a record J_{sc} exceeding 30 mA cm[27]. However, this design method is limited by the constraints between the spectral redshift and the rise in the HOMO energy level, which is unfavorable for matching with high-performance donors leading to the moderate V_{oc} and FF[28]. Herein, we design an asymmetric NFA P2EH-1V by unidirectionally extending the conjugation of P2EH[29-30]. Introducing double bonds into the acceptor molecules can significantly increase the conjugation length, forming a larger π-conjugated system, thereby enhancing the delocalization of electrons[31-32]. In π-conjugated systems, electrons in the π orbitals are delocalized across the conjugated structure. By extending the conjugation by inserting double bonds, the electron density spreads over a larger area, leading to a reduction in the energy gap between lowest unoccupied molecular orbital (LUMO) and HOMO [33-34]. The molecular structures of P2EH, P2EH-1V and P2EH-2V are shown in Fig. 1a. Figure 1b and Supplementary Fig. 1 show the normalized UV–vis absorption spectra of the three NFA films and solutions. Supplementary Fig. 2 shows the absorption coefficient of neat and blend film. As reported previously, P2EH shows an absorption onset of 890 nm and an optical band gap of 1.39 eV. The absorption of P2EH-1V is redshifted about 80 nm compared with that of P2EH, corresponding to the optical band gap of 1.27 eV. Due to the further increased conjugation length, the absorption onset of P2EH-2V is redshifted to 1033 nm with the bandgap of 1.20 eV. P2EH-1V and P2EH-2V deliver red-shifted absorption spectrum, which can broaden the light-harvesting window for higher J_{sc} in perovskite-organic tandem cells.

Unlike the NFA P2EH-2V, where double bonds are inserted on both sides, inserting double bonds unidirectionally allows for more precise control of the rise in the HOMO

energy level. Cyclic voltammetry measurements are performed to estimate the electronic energy levels of the PM6 (PBDB-T-2F) and 3 NFAs. As expected, with the increase in the number of double bonds of the NFAs, the HOMO energy level gradually rises. The HOMO energy level / LUMO energy level values of PM6, P2EH, P2EH-1V and P2EH-2V are measured to be −5.49/–3.55, −5.73/–3.90, −5.55/–3.96 and −5.39/–4.00 eV, respectively (Figure 1c, Supplementary Table 1 and Supplementary Fig. 3). Compared to P2EH, the HOMO energy level of P2EH-1V appropriately reduces the bandgap, while ensuring the exciton dissociation driving force. A negative donor-acceptor offset is found between PM6 and P2EH-2V, which could result in a poor hole transfer process[35].

The crystalline behaviors of the different NFAs based films are characterized by the grazing-incidence wide-angle X-ray scattering (GIWAXS). A detailed explanation of radial GIWAXS profiles is provided in Supplementary Notes 1. All acceptors exhibit a preferential face-on orientation with comparable coherence lengths (CCL), as shown in Supplementary Figures 4 and 5. For PM6:NFA blends (Fig. 1d and Supplementary Fig. 6), the coherence lengths of the (010) diffraction peaks for the three blended films are comparable. These consistent CCL values indicate that introducing double bonds into P2EH does not significantly disrupt the packing of the original ordered acceptors. This underscores the potential of P2EH-1V to achieve a comparable FF to P2EH while simultaneously reducing the bandgap[36]. The subtracted parameters from 2D GIWAXS images are summarized in Supplementary Table 2-3. The surface morphology for the different blends is evaluated by atomic force microscopy (AFM) as displayed in Supplementary Fig. 7. The active layers based on the three acceptors exhibit similar surface roughness. Contact angle measurements indicate that compatibility decreases as the number of double bonds in the acceptor increases (Supplementary Fig. 8 and Supplementary Table 4). TEM analysis further reveals that increasing the number of double bonds results in more pronounced phase separation between the donor and acceptor in the active layers. For the PM6:P2EH-1V blend films, marginally larger bright and dark patterns are observed compared to the PM6:P2EH blend films. In contrast, much more pronounced bright and dark patterns are evident in the PM6:P2EH-2V blend films. These findings suggest that PM6:P2EH-1V blend films remain within a favorable phase separation regime, which promotes efficient exciton dissociation, whereas PM6:P2EH-2V blend films exhibit excessive phase separation (Supplementary Fig. 9).

To take advantage of superiorities brought by the broader absorption range of P2EH-1V, we fabricate single-junction organic solar cells based on structure of indium tin oxide (ITO)/MoO_x/PM6:NFA/PDINN/Ag. Fig. 1e shows the champion *J-V* characteristics and Supplementary Table 5 summarizes their photovoltaic parameters. The device based on PM6:P2EH achieve a maximum PCE of 17.5% with a V_{oc} of 0.88 V, J_{sc} of 25.72 mA cm^{-2} and an FF of 77.2%. Encouragingly, the PM6:P2EH-1V based OSC achieve a PCE of 17.9% with V_{oc} of 0.82 V, a higher J_{sc} of 28.60 mA cm^{-2} and FF of 76.5%. The enhanced J_{sc} resulted from the obviously red-shifted absorption of P2EH-1V. Though the absorption spectrum of P2EH-2V is further broadened, the

device shows a much lower PCE of 5.6% with low J_{sc} of 11.21 mA cm^{-2} and FF of 64.8%, which can be ascribed to HOMO level mismatch with PM6. The photovoltaic parameters statistics and corresponding external quantum efficiency (EQE) plots of P2EH, P2EH-1V and P2EH-2V devices are displayed in Supplementary Fig. 10 and Fig. 1f. The integrated current densities derived from EQE plots are 25.12, 27.86, and 11.06 mA cm^{-2}, respectively, which match well with those afforded by *J-V* tests (within 3% error). Compared to previous reports of NFAs used in perovskite-organic tandem cells, as summarized in Figure 1g and Supplementary Table 6, P2EH-1V demonstrates superior optical bandgap and photovoltaic performance, making it a promising acceptor for constructing the bottom cell in perovskite-organic tandem cells.

To further assess charge dynamics of different blends, we utilize femtosecond transient absorption spectroscopy measurement to evaluate the hole transfer process from NFAs to donor[37-38]. The negative signals at 500-670 nm can be assigned to the ground state bleaching (GSB) of PM6, where no GSB signals are observed from the neat acceptor films (Fig. 2a-c and Supplementary Fig. 11-13). Here, GSB kinetics of PM6 are utilized on behalf of hole transfer dynamics, which mainly adopts the interfacial CT-state dissociation. Therefore, the hole transfer process can be assessed by fits to the donor GSB (575 nm) traces with a double exponential function, as displayed in Fig. 2d. For PM6:P2EH and PM6:P2EH-1V blends, prominent bleaching signals emerge in both blends. This observation indicates a rapid and efficient hole transfer process from the acceptor to the donor, which is consistent with the high EQE response for both cases. In contrast, very weak GSB signals appear in the PM6:P2EH-2V blend. This finding implies that the hole transfer from P2EH-2V to PM6 is minimal. The potential barrier between the HOMO levels of P2EH-2V and PM6 leads to a much slower hole transfer rate compared to PM6:P2EH-1V. This behavior suggests that the hole transfer from the acceptor P2EH-2V to the donor PM6 is negligible.

The charge dissociation probability (P_{diss}) for all devices is calculated from the photo-induced current density against effective voltage plots (Figure 2e). The PM6:P2EH and PM6:P2EH-1V -based devices exhibit the highest P_{diss} of 96.4% and 96.1%, enabling a high charge generation probability and consequently yielding the excellent EQE response. On the contrary, a low P_{diss} of 85.1% is observed in PM6:P2EH-2V -based device, which indicates the poor exciton dissociation behavior. The impedance spectroscopy results revealed that the P2EH and P2EH-1V based devices exhibit a significantly higher recombination resistance compared to P2EH-2V based device (Supplementary Fig. 14). This result indicates that the P2EH-2V-based device exhibits more severe charge recombination compared to the P2EH and P2EH-1V-based devices.

To investigate the influence of varying the number of π-bridges on the energy loss of NFAs, a detailed energy loss analysis is conducted (Fig. 2f-i), with the relevant data summarized in Fig. 2f and Supplementary Table 7. Compared to the P2EH-based device, the P2EH-1V-based device exhibited a 0.05 eV reduction in energy loss, primarily due to a decrease in non-radiative energy loss from 0.26 eV to 0.20 eV (Supplementary Fig. 15). Reducing the HOMO offset between the donor and acceptor effectively lowers non-radiative recombination[39-40]. However, in PM6:P2EH-2V, the negative HOMO

offset, while further suppressing non-radiative recombination, significantly hinders exciton dissociation and photocurrent generation. This phenomenon results from a shift in the CT–LE equilibrium towards the acceptor's LE states, leading to dominant recombination via the higher-emission LE states instead of the CT states[41], thereby reducing non-radiative energy loss. This result confirms that unidirectionally inserting π-bridges can effectively reduce the energy loss of the device while simultaneously broadening the photo-response.

Wide bandgap perovskite subcell

With all of the advantages discussed above, it is attractive to transfer the PM6:P2EH-1V bottom cell to perovskite-organic tandem cells. The expected most suitable bandgap for perovskite front cell should be around 1.8 eV. However, state-of-the-art wide-bandgap perovskite cells suffers from significant voltage and fill factor losses. To address these issues, we develop a self-assembled monolayer (SAM) of Br-Ph-4PACz by modification of Me-4PACz with introducing bromo-phenyl substitution instead of methyl substitution on the carbazole. The Br atom with strong electron affinity can effectively reduce work function and HOMO level, which can improve the band alignment with wide bandgap perovskites (Supplementary Fig. 16)[42]. Additionally, the steric hindrance of benzene ring can inhibit excessive aggregation of molecules, thereby enhancing the uniformity of the hole-transporting layer and perovskite growth[43].

We use ultraviolet photoelectron spectroscopy (UPS) to assess the energetic alignment of 1.8 eV perovskites and SAMs (Fig. 3b, Supplementary Fig. 17 and Supplementary Table 8)[44]. Br-Ph-4PACz features a significantly deeper work function and a favorable energy alignment with the perovskite, compared to the Me-4PACz, which can lead to a mitigated energy loss at the interface for the solar cell devices. Kelvin Probe Force Microscopy (KPFM) further corroborates the reduced work function of Br-Ph-4PACz on ITO substrate (Supplementary Fig. 18).

We conduct steady-state photoluminescence (PL) measurements, and as shown in Fig. 3c, the perovskite film on Br-Ph-4PACz exhibits a photoluminescence intensity that is five times higher than the perovskite film on Me-4PACz, suggesting reduced non-radiative recombination in the perovskite. Additionally, we calculate the PL quantum yield (PLQY) for both conditions, revealing a significant increase from 0.41% for the Me-4PACz based film to 1.82% for the Br-Ph-4PACz based film. We also extract quasi-fermi level splitting (QFLS) and Pseudo-*JV* of perovskite on different SAMs, which is directly related to the V_{oc} of device (Fig. 3d, e and Supplementary Fig. 19-21). Perovskite on Br-Ph-4PACz shows an implied open-circuit voltage (iV_{oc}) of 1.38 V, which is higher than that in perovskite/Me-4PACz stack (1.34 V), indicating a lower voltage loss at the interface between Br-Ph-4PACz and perovskites. Moreover, the Br-Ph-4PACz based device shows a shorter photocurrent decay lifetime of 0.73 μs than the Me-4PACz based device (0.87 μs), indicating improved charge carrier extractions in the Br-Ph-4PACz based device (Figure 3f).

We measure contact angles to study the wetting properties of the different SAMs (Supplementary Fig. 22). The Br-Ph-4PACz based substrate shows a significantly

decreased contact angle of 10.4°, compared to Me-4PACz (24.4°), indicating that the Br-Ph-4PACz enabled better wetting for uniform coverage of the perovskite film. We conduct confocal photoluminescence mapping to assess the uniformity of perovskite deposited on different SAMs. The results show that the perovskite film on Br-Ph-4PACz exhibits an improved photoluminescence emission intensity and homogeneity (Fig. 3g). This result suggests a significant enhancement in both the uniformity and optoelectronic quality of perovskite grown on Br-Ph-4PACz.

To take advantage of superiorities brought by the reduced voltage loss and improved uniformity, we fabricate single-junction wide-bandgap (WBG) perovskite solar cells. Fig. 3i and Supplementary Fig. 23 show the *J-V* curve of both 0.05 cm^2 Me-4PACz and Br-Ph-4PACz-based devices. Br-Ph-4PACz based devices show a champion PCE of 20.4%, with a high V_{oc} of 1.37 V and FF of 85.5%. The statistical distributions of these devices agreed well with better PCE (Supplementary Fig. 24). On the contrary, the Me-4PACz-based devices show moderate V_{oc} and FF of 1.33 V and 83.3%, resulting in a PCE of 19.2%. Results of EQE measurements show high EQE response of both devices and are in line with J_{sc} values obtained from *J-V* scans (Supplementary Fig. 25).

To further investigate the stability of wide-bandgap perovskites based on the different SAMs, we firstly tracked the evolution of PL spectra for both conditions by exposing PVK films to continuous 1-sun 532 nm laser illumination (Supplementary Fig. 26). After 10 minutes of continuous illumination, both wide-bandgap perovskite thin films on the two SAMs exhibited phase segregation, as evidenced by the emergence of a new PL peak centered at approximately 760 nm. Compared to Me-PACz-based films, the phase segregation in Br-Ph-4PACz-based films is notably mitigated, as evidenced by the significantly lower intensity of the new PL peak at 760 nm in Br-Ph-4PACz-based films. This result suggests a more homogenous growth and higher quality of the perovskite layer on Br-Ph-4PACz, which could reduce the halide segregation of perovskite film. The AFM results show that Br-Ph-4PACz-based films exhibit a more uniform surface morphology, with a lower root-mean-square (RMS) roughness of 18.9 nm, compared to the higher RMS roughness of 22.2 nm observed in Me-4PACz-based films, indicating better film quality of the perovskite layer on Br-Ph-4PACz (Supplementary Fig. 27). Furthermore, we also tested the long-term stabilities of wide bandgap perovskite devices at maximum power point (MPP) under illumination from a 100 mW cm^{-2} white LED at ambient atmosphere (Supplementary Fig. 28). The T_{80} of the Me-4PACz based device measured to be approximately 280 hours. However, the T_{80} of the device with Br-Ph-4PACz could be extended to 550 hours, suggesting the positive effect of suppressed phase segregation on the MPP stabilities of WBG PSC devices.

Perovskite-organic tandem solar cells

Encouraged by the broadened absorption of the bottom cell and the good homogeneity of the front cell, we fabricate perovskite-organic tandem with the device architecture of glass/ITO/SAM/perovskite/C_{60}/SnO_x/ITO/MoO_x/organic/PDINN/Ag. The thicknesses of the perovskite and organic absorber layers for the front and bottom subcells were

optimized to be approximately 290 and 110 nm (Fig. 4a), respectively, to obtain a well-balanced current density between the sub-cells. Figure 4b and Supplementary Fig. 29 presents the *J-V* curves of best performance perovskite-organic tandems with different organic absorbers (PM6:P2EH and PM6:P2EH-1V). The statistical results also show that the significant increase in J_{sc} is the main factor for the improvement in efficiency (Figure 4c and Supplementary Fig. 30). Notably, compared to the PM6:Y6 based device the PM6:P2EH-1V based device also boosts the efficiency from 25.8% to 27.5% with a V_{oc} of 2.14 V, J_{sc} of 15.37 mA cm^{-2} and FF of 83.7% (Supplementary Fig. 31). This value is the highest PCE reported for perovskite-organic tandem cells so far. The integrated J_{sc} values from EQE measurements for the top and bottom cells are 15.20 mA cm^{-2} and 15.14 mA cm^{-2} (Fig. 4d), in good agreement with the J_{sc} determined from *J–V* measurements. Notably, P2EH-1V exhibits significantly broadened near-infrared absorption and achieves a markedly higher integrated J_{sc}. Additionally, we also demonstrate a PCE of 26.7% V_{oc} of 2.14 V, J_{sc} of 15.15 mA cm^{-2} and FF of 82.4% for perovskite-organic tandem with an active area of 1.019 cm^2 (Supplementary Fig. 32), showing great potential for scaling up. We also sent the 1 cm^2 device to an accredited independent PV calibration laboratory (Shanghai Institute of Microsystem and Information Technology, SIMIT) for certification, and a certified PCE of 26.4% is obtained with no hysteresis (Figure 4e, Supplementary Fig. 33), agreeing well with the value measured in-lab. In addition, maximum point tracking efficiency is also tested within 300 s continuous tracking, the 1cm^2 perovskite-organic tandem device can still achieve a stabilized PCE of 26.5% (Figure 4f). As displayed in Fig. 4g and Supplementary Table 9, this certified PCE surpasses all certified PCEs for centimeter-scale single-junction perovskite solar cells, perovskite-CIGS tandem cells and perovskite-organic tandem cells.

We also evaluate the long-term stability of perovskite-organic tandem cells in ambient atmosphere (25°C, 85% relative humidity), which is harsher than ISOS-L-1 protocols (Fig. 4h). The encapsulated perovskite-organic tandem cells retain 80% of its initial efficiency after 783 hours of maximum power point tracking under continuous one-sun LED illumination at a relative humidity of 85%. The T_{80} of the single-junction OPV is only 180 hours (Supplementary Fig. 34), demonstrating the potential of tandem structures in improving OPV stability. This improvement is primarily due to the UV-filtering effect of the front wide-bandgap perovskite layer, which reduces the degradation of organic materials caused by high-energy photons. To achieve longer stability, strategies such as suppressing the phase segregation in wide bandgap perovskite, stabilizing the bulk heterojunction morphology and developing robust interfacial layers for organic subcells, will be pursued in the future.

References

1. Brinkmann, K.O., Wang, P., Lang, F. *et al.* Perovskite–organic tandem solar cells. *Nat Rev Mater* **9**, 202–217 (2024).

2. Brinkmann, K. O. et al. Perovskite–organic tandem solar cells with indium oxide interconnect. *Nature* **604**, 280–286 (2022).
3. Chen, W. et al. Monolithic perovskite/organic tandem solar cells with 23.6% efficiency enabled by reduced voltage losses and optimized interconnecting layer. *Nat. Energy* **7**, 229–237 (2022).
4. Lin, Y.*, et al.* An Electron Acceptor Challenging Fullerenes for Efficient Polymer Solar Cells. *Adv. Mater.* **27**, 1170-1174 (2015).
5. Meng, L.*, et al.* Organic and solution-processed tandem solar cells with 17.3% efficiency. *Science* **361**, 1094-1098 (2018).
6. Chen, W. et al. A semitransparent inorganic perovskite film for overcoming ultraviolet light instability of organic solar cells and achieving 14.03% efficiency. *Adv. Mater.* **30**, 1800855 (2018).
7. Zhang, Z., Chen, W., Jiang, X. *et al.* Suppression of phase segregation in wide-bandgap perovskites with thiocyanate ions for perovskite/organic tandems with 25.06% efficiency. *Nat Energy* **9**, 592–601 (2024).
8. Chen, X. et al. Efficient and reproducible monolithic perovskite/organic tandem solar cells with low-loss interconnecting layers. *Joule* **4**, 1594–1606 (2020).
9. Wang, X. et al. Highly efficient perovskite/organic tandem solar cells enabled by mixed-cation surface modulation. *Adv. Mater.* **35**, 2305946 (2023).
10. Ho-Baillie, A. W. Y. et al. Recent progress and future prospects of perovskite tandem solar cells. *Appl. Phys. Rev.* **8**, 041307 (2021).
11. Jiang, X., Qin, S., Meng, L. et al. Isomeric diammonium passivation for perovskite–organic tandem solar cells. *Nature* **635**, 860-866 (2024).
12. Chen, H., Liu, C., Xu, J. et al. Improved charge extraction in inverted perovskite solar cells with dual-site-binding ligands. *Science* **384**, 189-193 (2024).
13. Wang, Y., Lin, R., Liu, C. *et al.* Homogenized contact in all-perovskite tandems using tailored 2D perovskite. *Nature* **635**, 867–873 (2024).
14. Jost, M., Köhnen, E., Al-Ashouri, A. et al. Perovskite/CIGS tandem solar cells: from certified 24.2% toward 30% and beyond. *ACS Energy Lett.* **7**, 1298-1307 (2022).
15. He, Z., Yu, R., Dong, Y. et al. Minimized optical/electrical energy loss for 25.1% monolithic perovskite/organic tandem solar cells. *Nat. Commun.* **16**, 1773 (2025).
16. Wu, S., Liu, M. & Jen, A. K. Y. Prospects and challenges for perovskite–organic tandem solar cells. *Joule* **7**, 484–502 (2023).
17. Yuan, J., Zhang, Y., Zhou, L. et al. Single-junction organic solar cell with over 15% efficiency using fused-ring acceptor with electron-deficient core. *Joule* **3**, 1140-1151 (2019).
18. Leijtens, T., Bush, K. A., Prasanna, R. et al. Opportunities and challenges for tandem solar cells using metal halide perovskite semiconductors. *Nat. Energy* **3**, 828-838 (2018).
19. Wang, J., Xue, P., Jiang, Y. et al. The principles, design and applications of fused-ring electron acceptors. *Nat. Rev. Chem.* **6**, 614-634 (2022).
20. Cheng, P. & Yang, Y. Narrowing the band gap: the key to high-performance organic photovoltaics. *Acc. Chem. Res.* **53**, 1218-1228 (2020).

21. Liu, W., Sun, S., Zhou, L. et al. Design of near-infrared nonfullerene acceptor with ultralow nonradiative voltage loss for high-performance semitransparent ternary organic solar cells. *Angew. Chem. Int. Ed.* **61**, e202116111 (2022).
22. Jia, Z., Qin, S., Meng, L. et al. High performance tandem organic solar cells via a strongly infrared-absorbing narrow bandgap acceptor. *Nat. Commun.* **12**, 178 (2021).
23. Chen, Z., He, C., Ran, P. et al. Ultrafast energy transfer from polymer donors facilitating spectral uniform photocurrent generation and low energy loss in high-efficiency nonfullerene organic solar cells. *Energy Environ. Sci.* **16**, 3373-3380 (2023).
24. Sun, C., Pan, F., Chen, S. et al. Achieving fast charge separation and low nonradiative recombination loss by rational fluorination for high-efficiency polymer solar cells. *Adv. Mater.* **31**, 1905480 (2019).
25. Liu, Y., Liu, B., Ma, CQ. *et al.* Recent progress in organic solar cells (Part I material science). *Sci. China Chem.* **65**, 224–268 (2022).
26. Yi, J., Zhang, G., Yu, H. et al. Advantages, challenges and molecular design of different material types used in organic solar cells. *Nat. Rev. Mater.* **9**, 46-62 (2024).
27. Jia, Z. et al. Near-infrared absorbing acceptor with suppressed triplet exciton generation enabling high performance tandem organic solar cells. *Nat. Commun.* **14**, 1236 (2023).
28. Qin, S., Lu, C., Jia, Z. et al. Constructing monolithic perovskite/organic tandem solar cell with efficiency of 22.0% via reduced open-circuit voltage loss and broadened absorption spectra. *Adv. Mater.* **34**, 2108829 (2022).
29. Zhang, J., Bai, F., Angunawela, I. et al. Alkyl-chain branching of non-fullerene acceptors flanking conjugated side groups toward highly efficient organic solar cells. *Adv. Energy Mater.* **11**, 2102596 (2021).
30. Kong, X., Zhang, J., Meng, L. et al. 18.55% efficiency polymer solar cells based on a small molecule acceptor with alkylthienyl outer side chains and a low-cost polymer donor PTQ10. *CCS Chem.* **5**, 841-850 (2023).
31. Hai, J., Luo, S., Yu, H. et al. Achieving ultra-narrow bandgap non-halogenated non-fullerene acceptors via vinylene π-bridges for efficient organic solar cells. *Mater. Adv.* **2**, 2132-2140 (2021).
32. Li, X., Huang, H., Bin, H. et al. Synthesis and photovoltaic properties of a series of narrow bandgap organic semiconductor acceptors with their absorption edge reaching 900 nm. *Chem. Mater.* **29**, 10130-10138 (2017).
33. Liu, W., Xu, X., Yuan, J. et al. Low-bandgap non-fullerene acceptors enabling high-performance organic solar cells. *ACS Energy Lett.* **6**, 598-608 (2021).
34. Shi, W. & Ma, H. Spectroscopic probes with changeable π-conjugated systems. *Chem. Commun.* **48**, 8732-8744 (2012).
35. Bertrandie, J., Han, J., De Castro, C. S. P. et al. The energy level conundrum of organic semiconductors in solar cells. *Adv. Mater.* **34**, 2202575 (2022).
36. Zhu, L., Zhang, M., Zhou, G. et al. Achieving 20.8% organic solar cells via additive-assisted layer-by-layer fabrication with bulk pin structure and improved optical management. *Joule* **8**, 3153-3168 (2024).

37. Li, S., Zhan, L., Sun, C. et al. Highly efficient fullerene-free organic solar cells operate at near zero highest occupied molecular orbital offsets. *J. Am. Chem. Soc.* **141**, 3073-3082 (2019).
38. Li, S., Zhan, L., Sun, C. et al. Highly efficient fullerene-free organic solar cells operate at near zero highest occupied molecular orbital offsets. *J. Am. Chem. Soc.* **141**, 3073-3082 (2019).
39. Xie, Y., Wang, W., Huang, W. et al. Assessing the energy offset at the electron donor/acceptor interface in organic solar cells through radiative efficiency measurements. *Energy Environ. Sci.* **12**, 3556-3566 (2019).
40. Xu, Y., Yao, H., Ma, L. et al. Tuning the hybridization of local exciton and charge-transfer states in highly efficient organic photovoltaic cells. *Angew. Chem. Int. Ed.* **59**, 9004-9010 (2020).
41. Classen, A., Chochos, C. L., Lüer, L. et al. The role of exciton lifetime for charge generation in organic solar cells at negligible energy-level offsets. *Nat. Energy* **5**, 711-719 (2020).
42. Yi, Z., Wang, W., He, R. et al. Achieving a high open-circuit voltage of 1.339 V in 1.77 eV wide-bandgap perovskite solar cells via self-assembled monolayers. *Energy Environ. Sci.* **17**, 202-209 (2024).
43. Wang, X., Li, J., Guo, R., Yin, X., Luo, R., Guo, D., et al. Regulating phase homogeneity by self-assembled molecules for enhanced efficiency and stability of inverted perovskite solar cells. *Nat. Photonics* **18**, 1269–1275 (2024).
44. Siekmann, J., Kulkarni, A., Akel, S., Klingebiel, B., Saliba, M., Rau, U. & Kirchartz, T. Characterizing the influence of charge extraction layers on the performance of triple-cation perovskite solar cells. *Adv. Energy Mater.* **13**, 2300448 (2023).

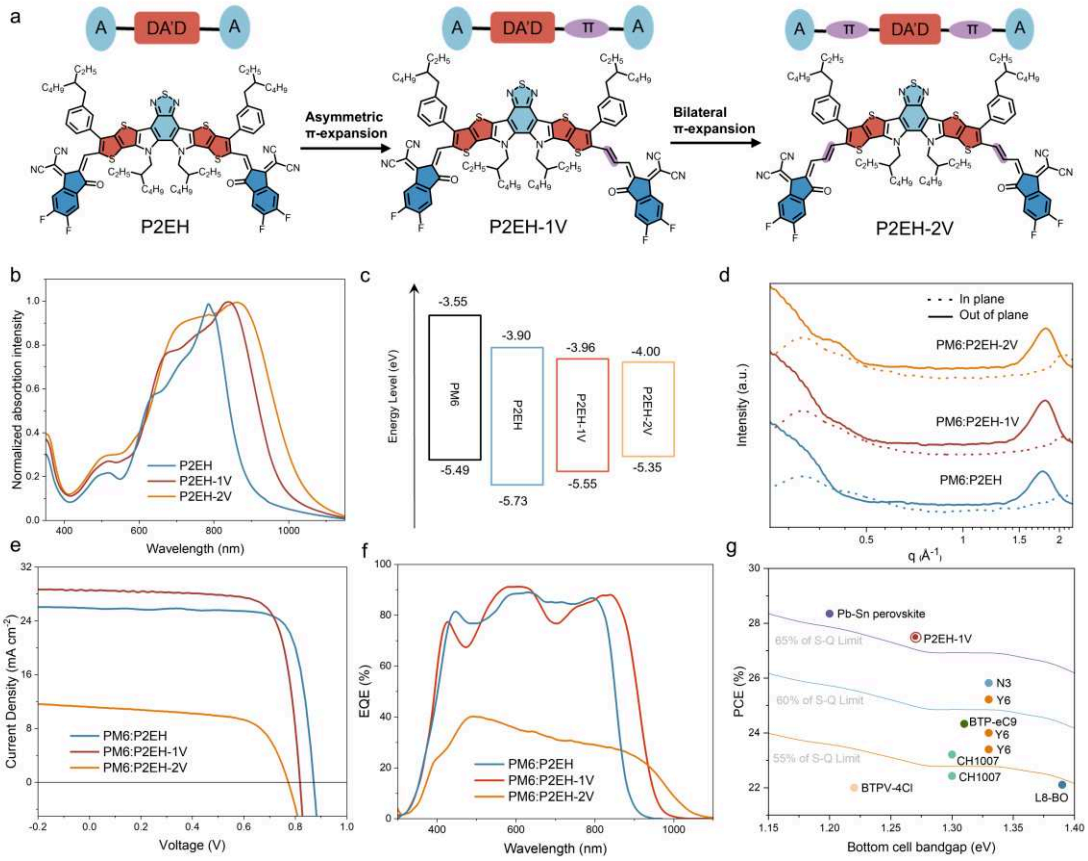

Fig. 1 Non-fullerene acceptor design and device performance. a, The molecular structure of acceptors. **b**, Absorption spectra of the P2EH, P2EH-1V and P2EH-2V films. **c**, The energy level diagram of PM6, P2EH, P2EH-1V and P2EH-2V neat films. **d**, Radial GIWAXS profiles integrated over in-plane ($30°<\chi<90°$) and out-of-plane ($0°<\chi<30°$) azimuthal angles for PM6:NFA blend films. **e**, Champion *J-V* curves of single-junction organic devices. **f**, EQE curves of single-junction organic devices **g**, Comparisons between champion perovskite-organic tandem cells of this work and previous reports of perovskite-organic tandem cells with a PCE≥22% in terms of optical bandgap of acceptor *vs* PCE.

Table 1 | Summary of photovoltaic parameters of champion single junction organic solar cell.

Active layer	V_{OC} / V	J_{SC} / mA cm^{-2}	FF / %	PCE / %
PM6:P2EH	0.88	25.72	77.2	17.5
PM6:P2EH-1V	0.82	28.60	76.5	17.9
PM6:P2EH-2V	0.77	11.21	64.8	5.6

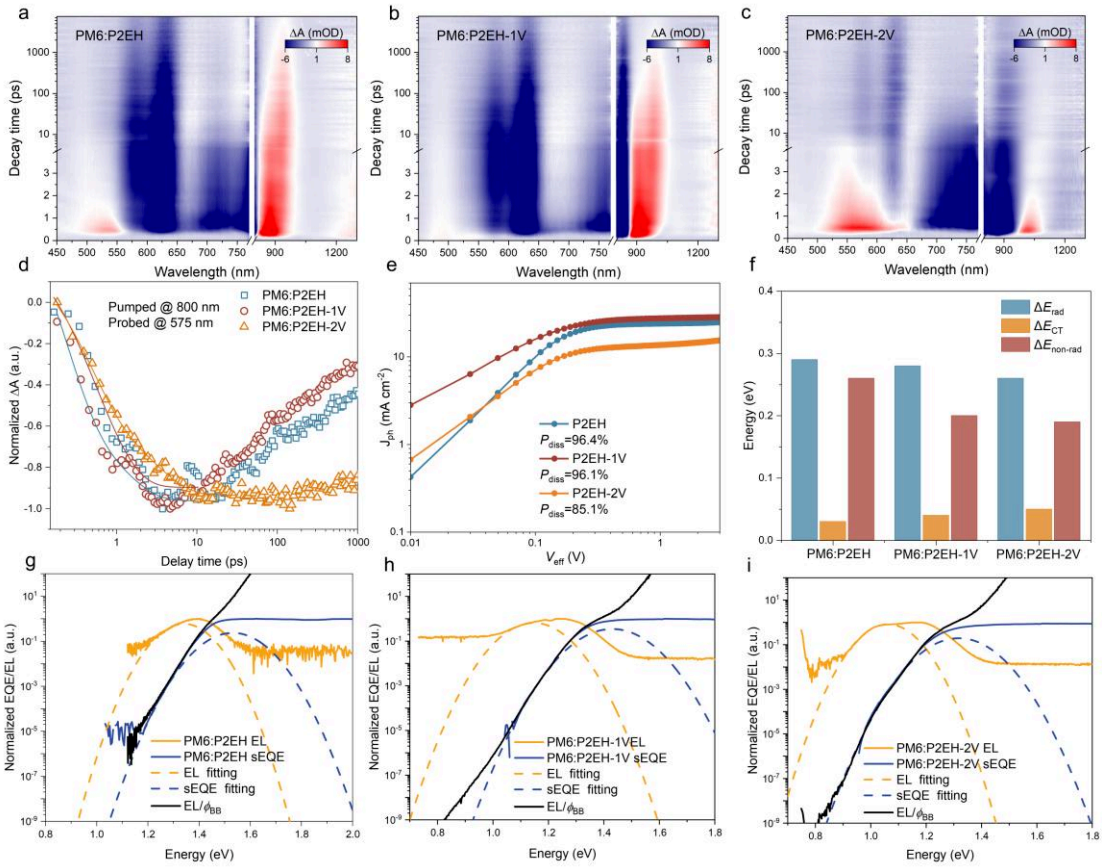

Fig. 2 | Charge dynamics and energy loss analysis. a,**b**,**c**, Femtosecond TA spectra of (**a**), PM6:P2EH (**b**), PM6:P2EH-1V (**c**) PM6:P2EH-2V blend film. **d**, the trace kinetic of donor GSB signal probed at 575 nm. **e**, Characteristics of the photocurrent density versus effective voltage ($J_{ph} - V_{eff}$). **f**, Summary of E_{loss} analysis of the corresponding OSCs. **g**,**h**,**i**, Gaussian fits of FTPS-EQE and EL curves via Marcus equation for devices based on (**f**) PM6:P2EH, (**g**) PM6:P2EH-1V, and (h) P PM6:P2EH-2V blend. **h**, Summary of E_{loss} analysis of the corresponding OSCs.

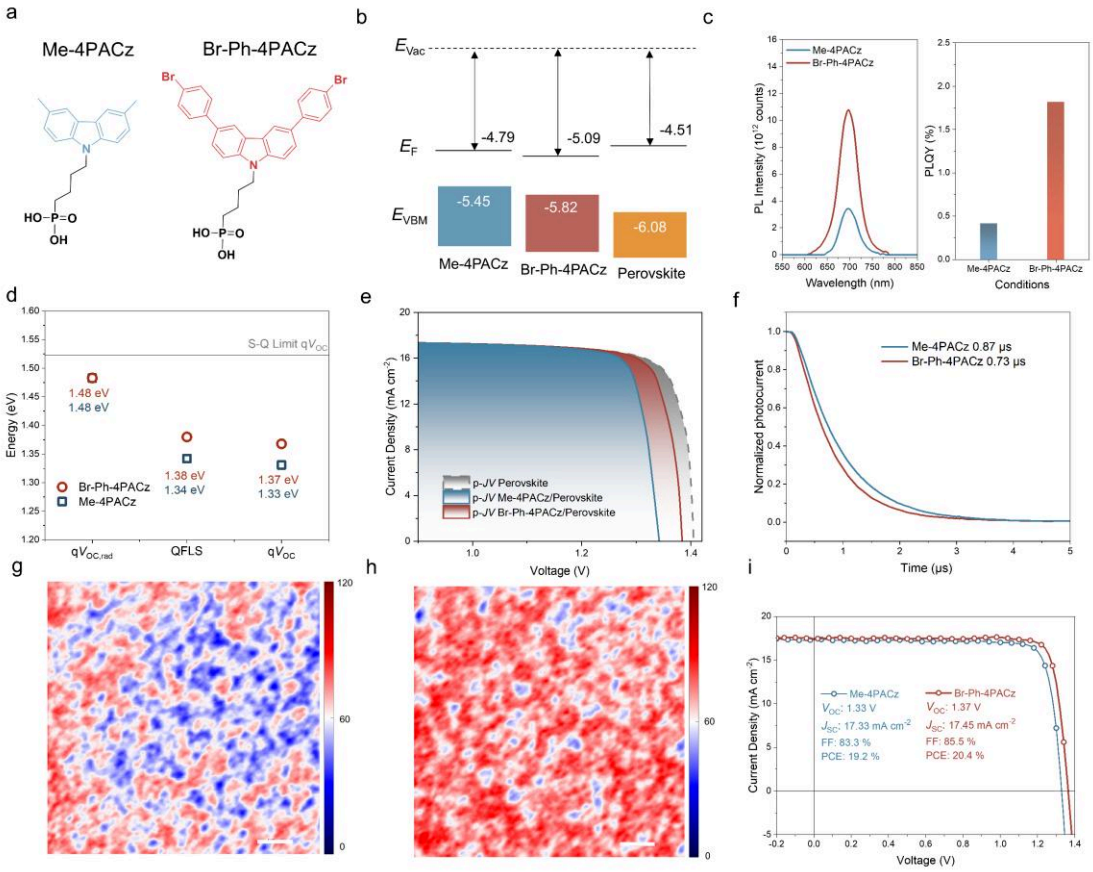

Fig. 3 | Single-junction WBG perovskite solar cells. a, Molecular structure of Me-4PACz and Br-Ph-4PACz. **b**, Energy band alignment between perovskite with Me-4PACz and Br-Ph-4PACz. **c**, Steady-state PL spectra of perovskite (left) and calculated PLQY comparison (right) for perovskite film on Me-4PACz and Br-Ph-4PACz. **d**, V_{oc} loss analysis for single-junction WBG perovskite solar cells. **e**, Pseudo-*JV* curves obtained from intensity-dependent V_{oc} and QFLS measurements on the neat perovskite, the SAMs/perovskite. **f**, Transient photocurrent (TPC) decays of Me-4PACz and Br-Ph-4PACz perovskite solar cells. The results are fitted with a single-exponential function. **g**, Confocal photoluminescence mapping images of perovskite film on Me-4PACz. **h**, Confocal photoluminescence mapping images of perovskite film on Br-Ph-4PACz. **i**, *J-V* scans of Me-4PACz and Br-Ph-4PACz perovskite solar cells.

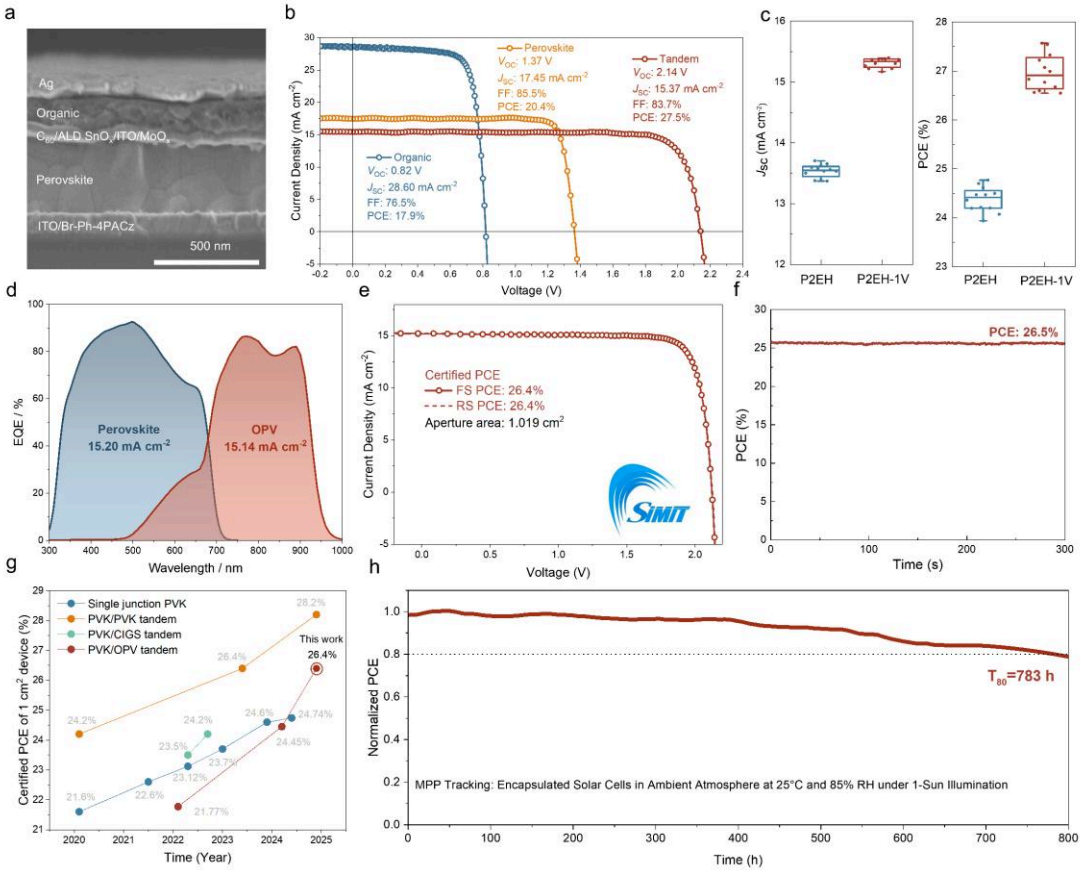

Fig. 4 | Perovskite-organic tandem cells with P2EH-1V and Br-Ph-4PACz. a, Cross-sectional SEM images of perovskite-organic tandem cells. **b**, Combination of champion *J-V* curves and photovoltaic parameters of single-junction OPV, perovskite solar cells and perovskite-organic tandem cells. **c**, Statistical distributions of J_{sc} (left) and PCE (right) of perovskite-organic tandem cells with different NFAs (12 devices for each type). **d**, EQE curves and integrated J_{sc} for perovskite and organic subcell in perovskite-organic tandem cells, respectively. **e**, *J-V* curves of the best 1 cm^2 perovskite-organic tandem cells certified by SIMIT. **f**, MPP tracking measurement of champion 1 cm^2 device. **g**, Summary of the reported, independently certified PCEs of centimeter-scale single-junction perovskite solar cells, perovskite-perovskite tandem cells, perovskite-CIGS tandem cells and perovskite-organic tandem cells. **h**, Long-term MPP tracking results of perovskite-organic tandem cells.

Methods

Materials. Cesium iodide (CsI, 99.999%), *N,N*-dimethylformamide (DMF, anhydrous), dimethyl sulfoxide (DMSO, anhydrous), methyl acetate (MeAc, anhydrous) and 2-propanol (IPA, anhydrous) were purchased from Sigma-Aldrich. Formamidinium iodide (FAI) was purchased from Greatcell Solar Materials. Lead iodide (PbI_2, 99.99%), lead bromide ($PbBr_2$) and [4-(3,6-Dimethyl-9H-carbazol-9-yl)butyl]phosphonic acid (Me-4PACz) were purchased from Tokyo Chemical Industry. Silver pellets were

purchased from Alfa Aesar and C_{60} and bathocuproine (BCP) were purchased from Luminescence Technology. PM6, Y6, P2EH and PDINN were purchased from Solarmer Material Inc. The synthetic routes of acceptor P2EH-1V, P2EH-2V and Br-Ph-4PACz are shown in Supplementary Fig. 36-46, respectively, and the detailed synthesis processes are described in the Supplementary Notes 2.

WBG perovskite single-junction device fabrication. The patterned indium tin oxide (ITO) glass substrates were cleaned with deionized water, acetone and IPA in the ultrasonic bath for 15 min each. After ultraviolet ozone treatment for 15 min, the substrates were transferred to a nitrogen-filled glovebox and the Me-4PACz or Br-Ph-4PACz solution (1 mg/ml in IPA) was spin-coated on the substrates at 4,000 r.p.m. for 30 s and heated at 100°C for 10 min. The 1 M perovskite ($Cs_{0.25}FA_{0.75}Pb(Br_{0.4}I_{0.6})_3$) precursor solution that were dissolved in 1 ml mixed solvent of DMF:DMSO (V/V = 4:1). Then the precursor solution was shaken for overnight at 60°C. For spin-coating process, the substrate was spinning at 3,000 r.p.m. for 60 s with an acceleration of 3000 r.p.m./s and 200 μL of MeAc was dropped at 15 s before the ending of spin-coating. To improve the wettability of the perovskite solution on Me-4PACz, we first dynamically spin-coated two small drops of perovskite solution at 4000 rpm. Unlike Br-Ph-4PACz, Me-4PACz required an additional 200 μL of precursor solution for better coverage. After dispensing, we removed the spin-coater chuck and gently shook the substrate, followed by spin coating process to form a uniform perovskite film. The perovskite films were then annealed at 100 °C for 15 minutes. 0.5 mg/mL $EDAI_2$ IPA solution was spin-coated onto the perovskite films at spin speed of 3000 r.p.m. for 30 s and annealed at 100 °C for 5 min. Lastly, C_{60} (20 nm)/BCP (8 nm)/Ag (100 nm) were deposited to complete the device fabrication.

Organic single-junction device fabrication. 15 nm MoO_x was thermally evaporated on top of ITO glass. Then the substrates were transferred into a glove box filled with nitrogen. The PM6: acceptor blend solutions (D:A = 1:1.2, 16 mg/mL in total, from CF solution with 10mg/ml 1-Bromo-3,5-dichlorobenzene as solid additive) with a total concentration of 16 mg/ml were heated at 40 °C till completely dissolved. The photovoltaic performance for different donor and acceptor concentrations are presented in Supplementary Table 9. Then the solutions were spin-coated at 3,000 r.p.m. for 30 s and annealed at 100 °C for 5 min. Then, 30 μL 1 mg/mL PDINN methanol solution was spin-coated onto the organic active layers at spin speed of 3000 r.p.m. for 30 s. Finally, the film was transferred to the thermal evaporator system to deposit 100 nm Ag as the top electrode.

Perovskite-organic tandem device fabrication. After completing the deposition of C_{60} layer, SnO_x (20 nm) was deposited by an atomic-layer deposition system. Then the substrates were transferred to the sputter system, where 5 nm ITO was sputtered. After then, 15 nm MoO_x was thermally evaporated on top of ITO and the film was brought back to the nitrogen-filled glovebox where organic ink was spin-coated at 3,000 r.p.m. for 30 s and annealed at 100 °C for 5 min. Next, PDINN was deposited by spin-coating its 1 mg/mL solution in methanol at 3,000 r.p.m. for 30 s. Finally, the film was

transferred to the thermal evaporator system to deposit 100 nm Ag as the top electrode to finish the tandem device fabrication process.

Device characterizations. Completed devices were masked with metal aperture masks (0.050 cm^2 and 1.019 cm^2) for *J–V* measurement by a Keithley 2400 source meter under simulated 1-sun AM 1.5G illumination (100 mW cm^{-2}) with an ABET Technologies Sun 2000 solar simulator in nitrogen-filled glovebox. The *J-V* measurements were performed in a N_2-filled glovebox. MPP stability tests of the devices were conducted by MPP Tracking-4B source measure unit system (Shenzhen Lancheng Technology Ltd.) under 100 mW cm^{-2} white LED in ambient atmosphere at a temperature of 25 °C and ~85% relative humidity with encapsulation. EQE measurements were conducted using a Bentham PVE300-IVT system, and the bias illumination obtained by 500 nm short wave pass filters and 800 nm long wave pass filters were used for the measurements of the bottom subcells and front subcells, respectively. The intensity of LED laser used was calibrated with built-in silicon and germanium diodes before measurements. For the HREQE tests, the light was chopped at 137 Hz and coupled into a Bentham monochromator. The monochromatic light spot was focused onto the active area of perovskite solar cell, and its current under short-circuit conditions was fed to a current preamplifier (Stanford SR 570) before it was analyzed with a lock-in amplifier (Stanford SR830 DSP). The time constant of the lock-in amplifier was chosen to be 1 s and the preamplifier's amplification was increased to resolve low photocurrents. The EQE was determined by dividing the photocurrent of the cell by the flux of incoming photons, which was measured using a calibrated Si photodiode. All EQE measurements were conducted in an ambient atmosphere with a temperature of 25 °C and ~60% relative humidity with encapsulation. Cross-sectional SEM images of devices were taken with Regulus SU8200 system (Hitachi) at 5 kV accelerating voltage under SE mode. The EL emission spectra were acquired by a combination of NOVA and NIR1700 spectrometers (Fuxiang Inc.). The voltage bias was applied to devices with a Keithley 2400 external voltage/current source meter. Sensitive-EQE was recorded by Fourier-transform photocurrent spectroscopy (PECT-600, Enli Technology Co., Ltd.). EQE_{EL} measurements were performed by applying external voltage/current sources through the devices (ELCT-3010, Enlitech).

Material characterizations. Steady-state PL and PL evolution measurements were done by LP20-32 radiative efficiency meter (Quantum Yield Berlin). The built-in 532 nm laser was switched on 15 min in advance to allow warmup and stabilization. All of PL spectra were recorded under 1-sun 532 nm laser illumination. Steady-state PL and PL evolution measurements were done by LP20-32 radiative efficiency meter (Quantum Yield Berlin). The built-in 532 nm laser was switched on 15 min in advance to allow warmup and stabilization. All of PL spectra were recorded under 1-sun 532 nm laser illumination. GIWAXS was conducted at TPS25A1 within National Synchrotron Radiation Research Center (NSRRC), Hsinchu. A monochromatic X-ray beam with an energy of 15 keV and a beam size of 5×5 μm^2 was used. The samples were probed at an incident angle of 0.16°. The sample-to-detector distance was 101.1 mm which was calibrated by a CeO_2 sample. The images were captured in two dimensions using a

single-photon counting detector, the Eiger X 1M, with a pixel size of 75 μm, and the obtained images were analyzed by INSIGHT software package. All samples were measured under a nitrogen-filled closed chamber. AFM measurements were performed with non-contact mode (NCM). Sideband KPFM measurements were performed under EFM (non-contact) mode. The work function was calibrated before every sample with a standard gold reference sample. Also, the signals were optimized in advance by applying bias voltage onto the samples in advance of the measurements.

AFM measurements were performed with non-contact mode (NCM). Sideband KPFM measurements were performed under EFM (non-contact) mode. The work function was calibrated before every sample with a standard gold reference sample. Also, the signals were optimized in advance by applying bias voltage onto the samples in advance of the measurements.

Femtosecond transient absorption (TA) spectra. Femtosecond transient absorption spectroscopy measurements were performed on an Ultrafast Helios pump-probe system in collaboration with a regenerative amplified laser system from Coherent. An 800 nm pulse with a repetition rate of 1 kHz, a length of 100 fs, and an energy of 7 mJ $pulse^{-1}$ was generated by a Ti: sapphire amplifier (Astrella, Coherent). Then the 800 nm pulse was separated into two parts by a beam splitter. One part was used as pump beam to excite the samples. The other part was focused onto a sapphire plate and a YAG plate to generate white light supercontinuum as the probe beams with spectra covering 420-800 nm and 750-1600 nm, respectively. The time delay between pump and probe was controlled by a motorized optical delay line with a maximum delay time of 8 ns. The pump pulse is chopped by a mechanical chopper with 500 Hz and then focused onto the mounted sample with probe beams. The probe beam was collimated and focused into a fiber-coupled multichannel spectrometer with CCD sensor. The energy of pump pulse was measured and calibrated by a power meter (PM400, Thorlabs). The films were spin coated onto the 1 mm-thick quartz plates and are encapsulated by epoxy resin in nitrogen-filled glove box to resist water and oxygen in air.

Data availability

The data that support the findings of this study are available from the corresponding authors upon request.

Acknowledgements

Y. Hou acknowledges the support from Agency for Science, Technology and Research (A*STAR) under its MTC IRG Grant (232K2087). Authors of this paper are affiliated with the Solar Energy Research Institute of Singapore (SERIS), a research institute at the National University of Singapore (NUS). SERIS is supported by the National University of Singapore (NUS), the National Research Foundation Singapore (NRF), the Energy Market Authority of Singapore (EMA) and the Singapore Economic Development Board (EDB). P.M.-B. acknowledges funding by the Deutsche Forschungsgemeinschaft (DFG, German Research Foundation) under Germany´s Excellence Strategy – EXC 2089/1 – 390776260 (e-conversion) and via TUM.solar in

the context of the Bavarian Collaborative Research Project Solar Technologies Go Hybrid (SolTech). The simulation works for this article were entirely performed on resources of the National Supercomputing Centre (NSCC) Singapore (https://www.nscc.sg). Part of this work was carried out at PETRA III, and we would like to thank Jinsheng Zhang, Altantulga Buyan-Arivjikh, Dr. Andrei Chumakov and Dr. Matthias Schwartzkopf for assistance in the measurements at the P03 beamline.

Author contributions

Z.J. and Y.H. conceived the idea and designed the experiments. Y.H. supervised the project. Z.J. synthesized and characterized the acceptors. Z.J. and X.G. fabricated and characterized perovskite-organic tandem cells. X.G. conducted device characterizations of WBG perovskite solar cells. M.S. and X.D. measured and analyzed the energy loss of organics. Q.J. and X.H. measured and analyzed transient absorption spectroscopy. Y.W. finished cross-sectional SEM imaging. J.H. finished TEM imaging. R.G., X.J., and C.K. performed GIWAXS measurements. S.R. and P.M.-B. provided resources of GIWAXS and supervision. Z.D. finished KPFM and AFM imaging. Y.W., X.W., Q.Z., X.J., J.C., Z.W., S.L., H.L., N.L., L.L. conducted material and photovoltaic characterizations for the perovskite solar cells. Z.S. contributed to DFT simulations. X.Y. synthesized the SAM material. Z.J. and Y.H. analyzed results and composed the manuscript. All authors discussed and polished the manuscript.

Competing interests

The authors declare no competing interests.